Analysis of a large seismically induced mass movement after the December 2018 Etna volcano (southern Italy) seismic swarm

Michele Saroli [a,b], Matteo Albano [b,*], Simone Atzori [b], Marco Moro [b], Cristiano Tolomei [b], Christian Bignami [b], Salvatore Stramondo [b]

[a] Dipartimento di Ingegneria Civile e Meccanica (DICeM), Università degli Studi di Cassino e del Lazio meridionale, via G. di Biasio 43, 03043 Cassino, FR, Italy
[b] Istituto Nazionale di Geofisica e Vulcanologia, via di Vigna Murata 605, 00143 Roma, Italy

ARTICLE INFO

ABSTRACT

In the recent decades, satellite monitoring techniques have enhanced the discovery of non-catastrophic slope movements triggered by earthquake shaking involving old paleo-landslides with deep-seated sliding surfaces. Understanding the triggering and attenuation mechanisms of such mass movements is crucial to assessing their hazard. In December 2018, Etna volcano (southern Italy) began a very intense eruption, which was accompanied by a seismic swarm with magnitudes reaching 4.9. Synthetic aperture radar data identified local displacements over a hilly area to the west of Paternò village. We evaluated the contribution of seismically induced surface instability to the observed ground displacement by employing a multidisciplinary analysis comprising geological, geotechnical and geomorphological data, together with analytical and dynamic modelling. The results allowed us to identify the geometry and kinematics of a previously unknown paleo-landslide, which was stable before the volcanic eruption. The landslide was triggered by the light-to-moderate seismic shaking produced by the strongest event of the seismic sequence, namely, the December 26, M_w 4.9 earthquake. This observation confirms that seismic shaking has a cumulative effect on landslides that does not necessarily manifest as a failure but could evolve into a catastrophic collapse after several earthquakes.

1. Introduction

Seismically induced landslides frequently accompany earthquakes (Bird and Bommer, 2004). Several case studies have been reported in which landslides, mainly rock falls, soil and rock slides, mudflows and rock avalanches, have been triggered by strong ground shaking (Rodríguez et al., 1999; Zhang, 2018 and references therein). The majority of these sliding phenomena involve the catastrophic collapse of the rock/soil mass (Roback et al., 2018). However, in recent decades, satellite monitoring techniques, such as the synthetic aperture radar Interferometry (InSAR), have allowed the discovery of non-catastrophic slope movements involving deep-seated sliding surfaces of old paleo-landslides (Albano et al., 2018, 2016; Casagli et al., 2017; Chen et al., 2014; Frattini et al., 2018; Huang et al., 2017; Moro et al., 2011; Polcari et al., 2017; Sato and Une, 2016). The triggering and attenuation mechanisms of such mass movements depend on several factors, such as seismic shaking intensity, geomechanical properties, and groundwater interactions (Bozzano et al., 2013; Esposito et al., 2007; Moro et al.,

2012). These factors govern the spatial extent and amplitude of the sliding mass displacement, which can evolve catastrophically after several seismic cycles. It is thus crucial to understand the factors triggering such sliding phenomena to assess their hazard.

An example of an earthquake-induced, non-catastrophic large mass movement was observed during the December 2018 Etna volcano (southern Italy) eruption (Bignami et al., 2019). On December 24, 2018, Etna volcano began a very intense eruption, featuring massive ash and gas emissions, lava flows, and a seismic swarm with magnitudes less than 5. Hundreds of earthquakes (Fig. 1) were associated with a dyke intrusion in the upper part of the Etna volcano, which induced significant deformation of the volcanic edifice (Bonforte et al., 2019; De Novellis et al., 2019). The dyke intrusion encouraged, with favourable stress loading, seismic dislocation of the Fiandaca Fault (Fig. 1) (De Novellis et al., 2019). A strike-slip earthquake (M_w 4.9) nucleated on December 26, 2018, at a focal depth of approximately 1 km, causing ground fractures and some damage to nearby villages (Villani et al., 2020).

Space-borne synthetic aperture radar (SAR) data provide stunning pictures of the displacement fields caused by volcanic eruptions and earthquake dislocations (Bignami et al., 2019; Bonforte et al., 2019; De Novellis et al., 2019). Fig. 1 shows the wrapped displacement observed in the period December 22–28, 2018 along the descending line of sight (LoS), that is the direction of the shortest path between a point on the Earth's surface and the SAR antenna. Each colour cycle, from black to white, corresponds to ground displacement of approximately 2.8 cm. One highly visible deformation pattern is located along Mt. Etna's flanks, where a bi-lobate interferometric fringe pattern highlights the deformation induced by dyke intrusion (Bonforte et al., 2019; De Novellis et al., 2019). A second deformation pattern is localised to the S-E of Etna volcano, where small fringe pattern identifies the displacements caused by the December 26, M_w 4.9 strike-slip dislocation of the Fiandaca Fault (De Novellis et al., 2019).

Local small interferometric fringes identify a third deformation pattern over a hilly area located approximately 5 km west of Paternò village (the dashed black box in Fig. 1) (Bignami et al., 2019). This displacement is not related to volcanic inflation or fault dislocation, because no large earthquakes have occurred nearby (Fig. 1). Bignami et al. (2019) interpreted this displacement as potentially associated with the seismic reactivation of a paleo-landslide. Indeed, several geomorphological features are recognisable in the area, such as double crest lines, scarps, counterscarps, trenches, and depression alignments, which are typical indicators of the presence of active or quiescent mass movements. However, the epicentre of the strongest event of the sequence, i.e., the December 26, 2018, M_w 4.9 earthquake, took place at more than 20 km distance and produced negligible seismic shaking over this area, with peak ground accelerations of approximately 0.01 g (D'Amico et al., 2020).

Most earthquake-induced landslides are triggered by earthquakes of moderate to high magnitude, i.e., greater than 5 (Keefer, 1984). The larger an earthquake is, the more likely it is to trigger ground movements at a long distance from the epicentre (Keefer, 1984; Rodríguez et al., 1999). Generally, an M_w 4.9 event does not trigger landslides at distances more than 5–10 km (Keefer, 1984). However, this threshold should be considered with caution because it does not consider other factors affecting the slope stability, such as slope geometry, strength, and interaction with groundwater.

We conducted a multidisciplinary analysis comprising seismological, geological, geomorphological and remote sensing data, together with analytical and dynamic models, to unveil the phenomena that caused the observed ground displacements. Our analysis confirmed that the displacements detected by SAR data were caused by the undrained seismic instability of a previously unknown paleo-landslide. This result confirms that even light to moderate shaking can trigger landslide movement in specific geometrical and geomorphological conditions. In this case, earthquake shaking caused the undrained instability of a large mass whose slip surface was favourably oriented with the earthquake epicentre.
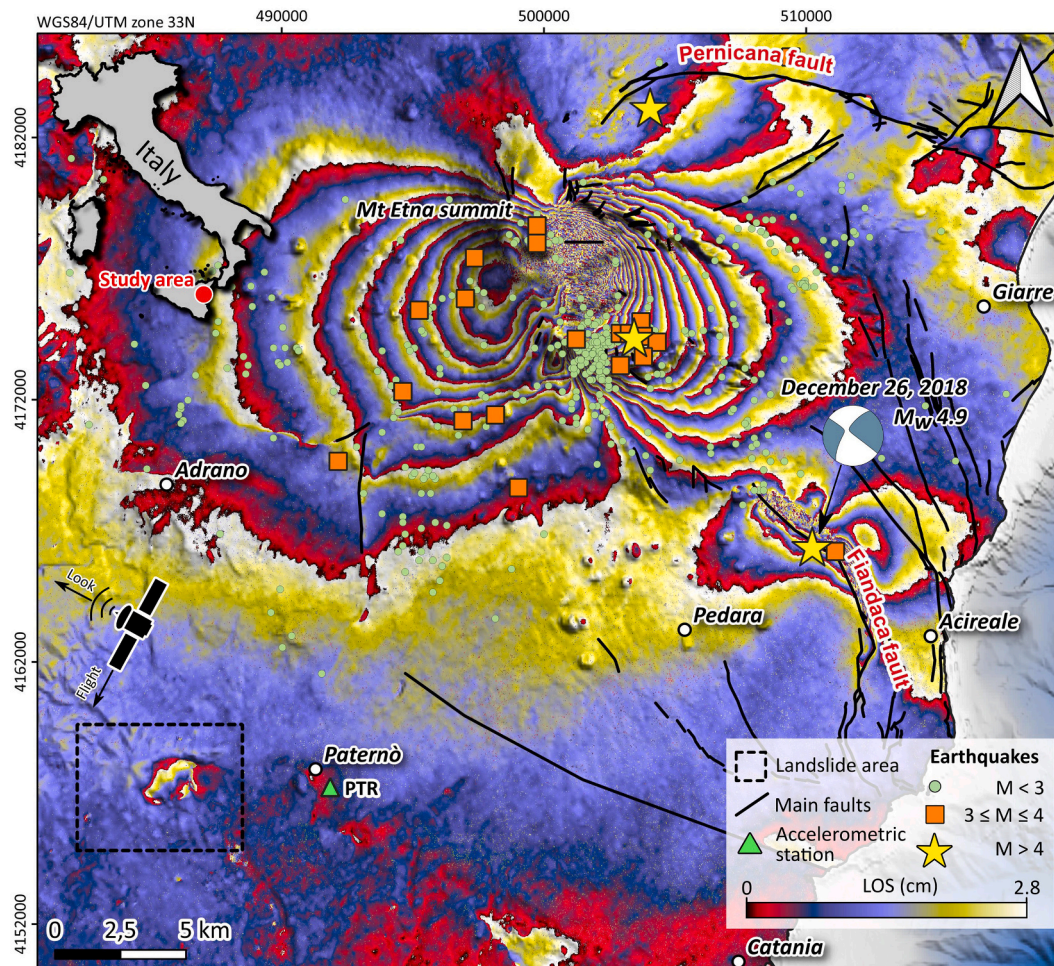

Fig. 1. Sketch of the Etna volcano area. The coloured pattern identifies wrapped ground displacements from the Sentinel-1 descending interferogram (22/12/2018–28/12/2018), and highlights the deformations caused by the Mt. Etna volcanic inflation, the December 26 M_w 4.9 earthquake along the Fiandaca Fault, and the mass movement to the west of Paternò village. The earthquake sequence reported in the figure (M_w > 1.5) was recorded from December 23, 2018, to January 30, 2019 (Berardi et al., 2020). The main faults are taken from Azzaro et al. (2013).

2. Data and methods

2.1. Geomorphological and lithological data

A detailed geomorphological analysis was conducted over the study area (the dashed black rectangle in Fig. 1). We exploited digital orthophotos at a 1:33000 scale from Volo Base survey in 1954-1955 and a LiDAR-derived digital elevation model (DEM) with 2 m × 2 m resolution provided by the Sicilia Region (available at http://www.sitr.regione.sicilia.it/). A geo-lithological analysis was also performed by exploiting Etna Volcano's Geological map (1:50000 scale) (Branca et al., 2011) and several in situ and laboratory investigations from the literature (Lo Verme and La Mendola, 2007; Vecchio, 2011) The latter consisted of grain size distributions, oedometric tests, shear-vane tests, and triaxial tests, which were exploited to retrieve the physical and strength properties of soils in the study area.

2.2. InSAR data and processing

Before, during, and after volcanic unrest, the ground deformation was investigated by exploiting several SAR image pairs acquired along both the ascending and descending passes by the Sentinel-1A/B (C-Band operated by ESA, hereinafter S-1) and ALOS-2 (L-Band operated by JAXA) satellite sensors. We exploited ten image pairs to assess the evolution of ground displacements over time, with revisit times of 6, 12 and 18 days for the ascending and descending S-1 datasets and 364 and 42 days for the ascending and descending ALOS-2 datasets, respectively (Supplementary Table S1 and Fig. S1). For each orbit pass, surface displacements were measured along the radar LoS. Displacements were retrieved with the differential SAR interferometry (DInSAR) technique (Massonnet and Feigl, 1998). DInSAR interferograms were generated on a 15 m ground-resolution cell for S-1 data and on a 25 m posting for ALOS-2 data. A 30 m digital elevation model (DEM) available from the shuttle radar topography mission (SRTM) (Farr et al., 2007) was exploited to remove the topographic phase contribution. Finally, the filtering approach of Goldstein and Werner (1998) was applied to unwrap the filtered interferogram employing the minimum cost flow algorithm (Costantini, 1998). The unwrapped pairs were then geocoded using the DEM.

All interferograms were processed using SARscape® software (Sarmap, CH, http://www.sarmap.ch/wp/) integrated into the ENVI environment (https://www.l3harrisgeospatial.com/Software-Technology/ENVI-SARscape) and currently consolidated two-pass interferometry analysis was adopted (Massonnet and Feigl, 1998; Pepe and Calò, 2017). The computed ascending and descending LoS measurements were then corrected with respect to possible orbital shifts or trends and combined to estimate the vertical and horizontal (east-west) ground displacement fields according to the equations in Dalla Via et al. (2012).

2.3. Earthquakes and strong-motion data

Seismological data included the hypocentral locations and magnitudes of earthquakes belonging to the seismic sequence from December 23, 2018, to January 30, 2019 (Fig. 1). For the strongest event of the sequence (the December 26, 2018, M_w 4.9 earthquake) we collected the PGA-based shakemap, which was provided by INGV (Faenza and Michelini, 2011, 2010), and the acceleration time history recorded at the Paternò seismic station (PTR in Fig. 1), which was available from the Italian Accelerometric Archive (D'Amico et al., 2020).

2.4. Back-analysis of slope movements

Multiple approaches are currently available to model slope dynamic performance, such as pseudostatic stability analysis, permanent displacement analysis, and advanced numerical simulations (Jibson, 2011). Pseudostatic stability analysis is simple, requires few data for calibration, and provides a straightforward scalar index of stability, the safety factor.

Permanent displacement analysis (Newmark, 1965) improves the simple pseudostatic approach by calculating earthquake-induced ground movements with little effort in terms of the required parameters. Numerical simulations allow geological and geometrical complexities and account for the full dynamic behaviour of soils affected by cyclic loads. However, they need a significant amount of data for calibration and are challenging to apply at medium to large scales. More sophisticated methods do a better job in modelling the dynamic response of the landslide material, potentially yielding more accurate displacement estimates, but there is a trade-off between the complexity of the analysis and the effort needed to acquire input parameters. Therefore, appropriate modelling approach is case-dependent; it depends on the scale of the problem and the requirements of the analysis.

We adopted a permanent displacement approach for our case study because it provides a reasonable estimate of earthquake-induced displacements with few required parameters. Indeed, such an approach has been successfully applied worldwide to earthquake-induced landslides involving soils or bedrock (Albano et al., 2018, 2016; Jibson, 1993; Jibson et al., 2000). In its simplest form, Newmark's permanent-displacement approach assumes that the landslide mass behaves as a rigid block that slides on an inclined plane (Fig. 2a). The amount of block displacement (δ) depends on the amplitude and frequency content of the applied strong-motion record and a critical acceleration parameter (a_c in Fig. 2b), the acceleration value that must be exceeded for the block to begin moving relative to its base (the blue curve in Fig. 2b). The parts of the acceleration record that exceed the a_c value (the grey areas in Fig. 2b) are integrated twice to obtain the velocity-time history (the green curve in Fig. 2b) and the cumulated displacement of the landslide block (δ) (the red curve in Fig. 2b). The higher the a_c value is, the lower the cumulative δ for the same seismic input.

The a_c value depends on the sliding mechanism and geometry (e.g., translational or rotational) and soil strength parameters: the effective friction and cohesion in the case of drained conditions (ϕ' and c' in Fig. 2c); or the undrained cohesion in the case of undrained conditions (c_u in Fig. 2c). The a_c value is commonly estimated by iteratively performing a pseudostatic limit-equilibrium analysis of the slope until finding an a_c value that yields a safety factor of 1 (Zhang, 2018), which indicates the onset of the slope instability.

This approach has been applied to investigate the interplay between slope movements observed through InSAR analysis and seismic shaking (Albano et al., 2018; Di Naccio et al., 2019). To this aim, we performed a back-analysis of the observed sliding mass movements. Back-analysing slope movements involves determining the shear strength of the soil mass, i.e., c', ϕ' or c_u in Fig. 2c, given the conditions that existed at the time of failure, such as the pore-water pressure distribution, the characteristics of the seismic load, and the geometry and slip of the sliding surface. The latter could be unknown in the case of non-catastrophic slope movement involving blind surfaces, as in this case study. To estimate the required parameters, we followed these steps:

i) Estimation of the geometry and slip distribution of the potential sliding surface by analytical inversion of the observed InSAR displacement, assuming a planar source embedded in an elastic medium;

ii) Assessment of the critical soil strength parameters by performing a pseudostatic limit equilibrium analysis of the slope, considering the slip of the sliding surface (δ), the seismic input and the critical acceleration (a_c) of the slope;

iii) Validation of the computed strength parameters by comparison with those provided by laboratory and in situ surveys.

2.4.1. Estimation of the geometry and slip distribution of the potential sliding plane

We derive the source responsible for the observed displacement through a process known as data inversion, where the cause is inferred
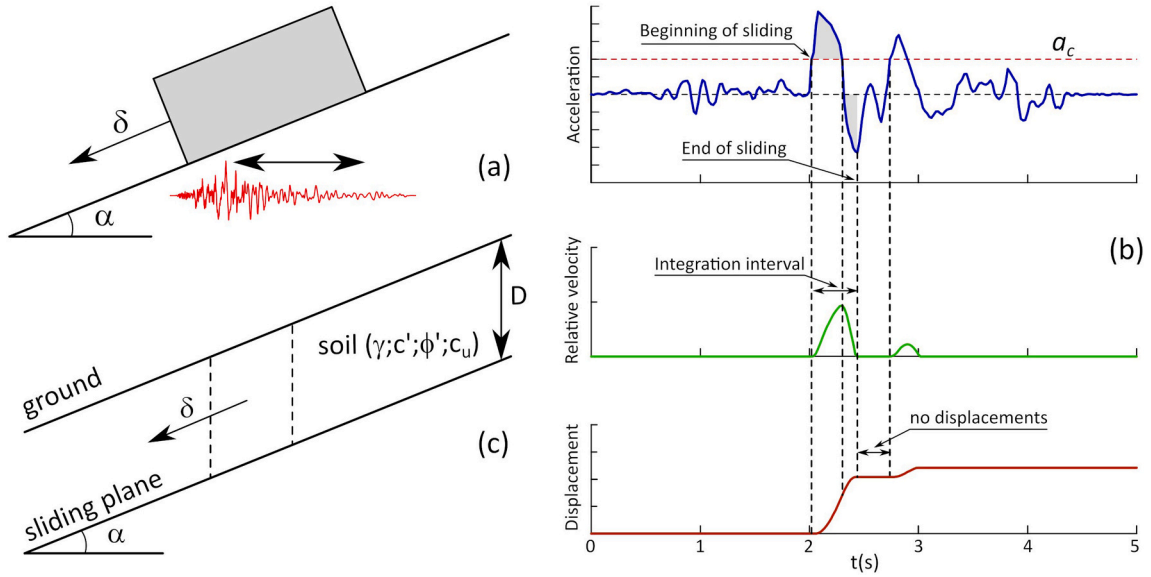
Fig. 2. (a) The Newmark (1965) scheme of a block resting on an inclined plane and subject to a horizontal acceleration time history. (b) Double integration scheme of the acceleration time history according to the Newmark sliding block approach. (c) Infinite slope scheme.

from its effect. The geometry and slip distribution of the potential sliding plane were retrieved by modelling the InSAR-derived ground displacements and assuming shear dislocation on a planar source embedded in an elastic and homogeneous half-space (Okada, 1992). This analytical approach is widely applied to infer the source geometry of a seismogenic fault after an earthquake (Albano et al., 2017; Polcari et al., 2018; Stramondo et al., 2016), and several publications have shown its effectiveness in modelling of non-catastrophic sliding phenomena involving deep sub-planar sliding surfaces (Aryal et al., 2015; Kang et al., 2019; Moro et al., 2011). This is possible by introducing corrections that modify the simple half-space to include the local topography, allowing the sliding surface to lie above the zero-level half-space surface (Williams and Wadge, 1998).

In addition to the analytical model, optimisation algorithms are adopted to constrain the source parameters (Atzori and Salvi, 2014). We carry out preliminary nonlinear optimisation based on the Levemberg-Marquardt algorithm (Marquardt, 1963) to identify the sliding surface geometry (dimension, position and inclination) assuming a uniform slip in a downhill direction. The optimisation must find the minimum of a cost function affected by additional local minima in the n-dimensional parameter space, as in all nonlinear problems. Therefore, the algorithm is implemented with multiple restarts to avoid the cost function becoming trapped in a local minimum. We also run uncertainty analysis to assess the best-fit configuration reliability by inverting 50 InSAR datasets perturbed with spatially correlated noise, according to Parsons et al. (2006) and Atzori et al. (2009).

After defining the sliding plane with a uniform shear slip, linear inversion is carried out to retrieve the slip distribution across it, thus providing a more reliable solution. This step is performed in a least-squares sense, as in the nonlinear case, with the additional condition of preventing negative slip values (unrealistic uphill movements).

A linear ramp's parameters are simultaneously assessed and removed for each InSAR dataset to minimize the impact of InSAR artefacts. The overall process is carried out with the SARscape® modelling tool.

2.4.2. Assessment of the critical soil strength parameters

The critical soil strength parameters are determined by performing a pseudostatic limit-equilibrium analysis assuming an infinite slope with a planar surface (Fig. 2c).

For a soil obeying the Mohr-Coulomb failure criterion, i.e., $\tau = c' + \sigma'$

$\tan \phi'$ and with a seepage flow oriented downslope, the pseudostatic factor of safety is given by:

$$F_s = \frac{c'}{\gamma D cos^2 \alpha \left[k_h + (1 \pm k_v) tan\alpha \right]} + \frac{1 \pm k_v - r_u - k_h \, tan\alpha}{k_h + (1 \pm k_v) \, tan\alpha} tan\phi' \quad (1)$$

where k_v (g) and k_h (g) are the horizontal and vertical pseudostatic seismic coefficients, respectively; γ (kN/m^3) is the natural unit weight of the soil; D (m) is the thickness of the sliding mass; α is the inclination of the sliding plane; r_u is a pore pressure coefficient; and ϕ' and c' are the soil friction angle and effective cohesion, respectively (Fig. 2c).

In the case of incipient collapse, $F_S = 1$. Thus, it is possible to resolve Eq. (1) with respect to the horizontal seismic coefficient k_h, neglecting the seepage forces ($r_u = 0$) and the vertical component of the seismic coefficient ($k_v = 0$):

$$k_h = k_c = \frac{c'}{\gamma D cos^2 \alpha \, (1 + tan\alpha \, tan\phi')} + \frac{tan\phi' - tan\alpha}{1 + tan\alpha \, tan\phi'} \quad (2)$$

where $k_h = k_c$ represents the critical horizontal seismic coefficient, the coefficient that triggers slope instability.

For a slope made of coarse-grained (permeable) material, excess pore pressures during seismic shaking are not expected, and the soil behaves similar to drained soil. Under such conditions, it is possible to resolve Eq. (2) with respect to the soil internal friction angle ϕ', assuming $c' = 0$, thus obtaining:

$$\phi'_c = tan^{-1} \frac{k_c + tan\alpha}{1 - k_c tan\alpha} \quad (3)$$

Eq. (3) provides the critical soil friction angle (ϕ'_c) as a function of the critical horizontal seismic coefficient (k_c) and the inclination of the sliding surface (α).

For a slope made of fine-grained (less permeable) material, it is reasonable to assume that the soil does not drain appreciably during earthquake shaking because of the earthquake's short duration. Therefore, seismic loading may increase the total stress at the base of a slice, and there may be an equivalent change in the pore pressure, but the effective stress remains unchanged. Under this condition, the soil behaves as undrained according to the Tresca failure criterion, $\tau = c_u$, where c_u is the undrained cohesion. Therefore, substituting $c' = c_u$ and $\phi' = 0$ into Eq. (2) and resolving it with respect to c_u gives:

$$c_{u,c} = (k_c + tan\alpha)\gamma Dcos^2\alpha \qquad (4)$$

Eq. (4) provides the critical undrained cohesion ($c_{u,c}$) as a function of the critical horizontal seismic coefficient (k_c), the soil unit weight (γ), the inclination of the sliding plane (α) and the thickness of the unstable slice (D).

In Eqs. (3) and (4), the critical seismic coefficient k_c is equivalent to the critical acceleration a_c of Fig. 2b, but is expressed in terms of the acceleration of gravity, $k_c = a_c/g$.

The critical acceleration values (a_c) (or equivalently the k_c values) for the Paternò landslide mass are estimated by assigning a range of a_c values and calculating the corresponding δ values with the Newmark displacement approach (Fig. 2b). The acceleration time history registered at the PTR accelerometric station is assumed to be the seismic
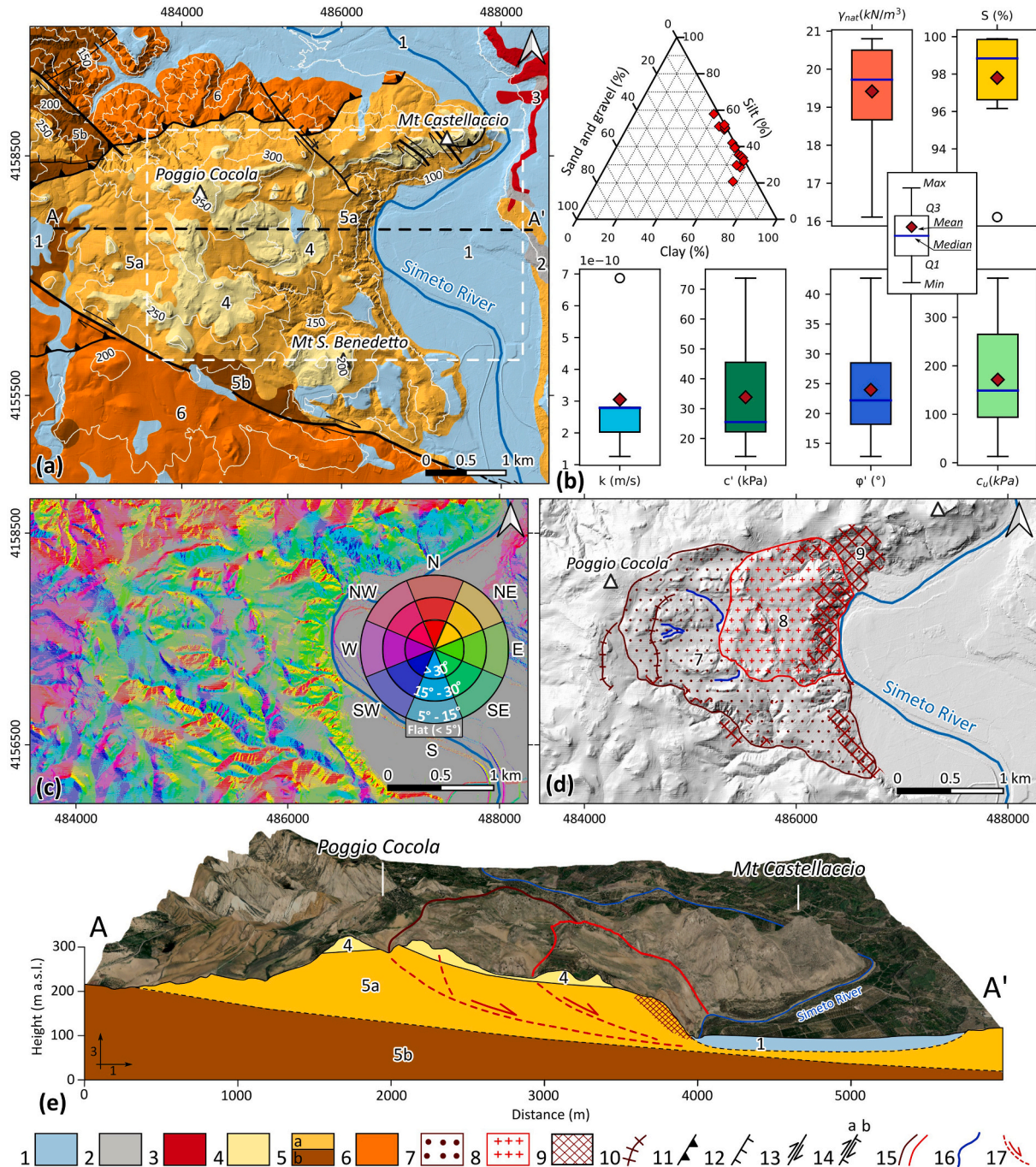
Fig. 3. Geo-lithological and geomorphological sketch of the study area. (a) Geo-lithological map; the dashed white box identifies the extent of panels c and d. (b) Main geotechnical parameters of the *Terravecchia* Formation: γ_{nat} = natural unit weight; S = water saturation percentage; k = hydraulic conductivity; c' = drained cohesion; ϕ' = drained friction angle; c_u = undrained cohesion. (c) Aspect-slope map of the study area; colours indicate the aspect; shades of grey indicate the slope in degrees. (d) Geomorphological map. (e) Geological cross-section along the A-A' profile in panel a. Key to the legend: 1. Recent and old terraced alluvial deposits (Holocene); 2. Travertine deposits (Holocene); 3. Lava flows, scoria cones and pyroclastic fall deposits (Pleistocene-Holocene); 4. Marly limestone and limestone breccias with gypsum (Messinian-lower Pliocene); 5a, b. *Terravecchia* formation (upper Tortonian); 6. Grey silty-marly clays with Numidian Flysch (Oligocene – Serravallian); 7. Outer DGSD body; 8. Inner DGSD body; 9. Areas affected by surficial landslides; 10. Linear trenches; 11. Thrust fault; 12. Normal fault; 13. Strike-slip fault. 14. Normal fault with lateral movement; 15. (a) Inner and (b) outer DGSD boundary; 16. Paleo-drainage; 17. Inferred DGSD sliding surface.

input. This approach provides an empirical a_c - δ curve from which it is possible to estimate the a_c values that correspond to the slip (δ) of the sliding plane retrieved from analytical inversion of the InSAR displacements (see paragraph 2.4.1).

3. Results

3.1. Geological, geomorphological and lithological features of the area

The investigated area (Fig. 3a) is part of the Gela fold, and represents the most external sector of the Apennines-Magrebides chain. The site is composed of proximal molassic deposits known in the literature as the *Terravecchia* Formation (upper Miocene), which developed in subsidiary basins and then was deformed in a wide synclinal fold delimited by compressive tectonic elements. It presents a thickness of approximately 300 m and consists of grey-blue and brown marly clays (5b in Fig. 3a), with brown brecciated clays near the top of the formation (5a in Fig. 3a) (Branca et al., 2011; Carbone et al., 2010).

Available in-situ and laboratory investigations classify the *Terravecchia* Formation as a slightly overconsolidated clay with silt or silt with clay, with a small percentage of sand and gravel (less than 15% in Fig. 3b). It has a mean unit weight of approximately 19.5 kN/m^3 (γ_{nat} in Fig. 3b), a degree of saturation of approximately 98% (S in Fig. 3b) and a hydraulic conductivity of approximately 3×10^{-10} m/s (k in Fig. 3b), which classifies this lithology as effectively impervious at the relevant time and length scales (Carbone et al., 2010). Its drained strength, expressed in terms of the effective cohesion and friction (c' and ϕ' in Fig. 3b), ranges between 25 and 45 kPa and 18–27 degrees, respectively. The undrained strength, expressed as the undrained cohesion (c_u in Fig. 3b), ranges between 90 and 270 kPa.

The study area presents a hilly morphology (Fig. 3c), with the *Mt. Castelluccio* (218 m a.s.l.), *Poggio Cocola* (345 m a.s.l.) and *Mt. S. Benedetto* (228 m a.s.l.) hills representing the primary relief. The topography gradually degrades from *Poggio Cocola* towards the E (Fig. 3c), with an average slope of approximately 10° - 15°, until a large escarpment reached at approximately 80 m a.s.l., with slopes greater than 30° produced by progressive erosion by the Simeto River. Photogeological analysis and the available high-resolution DEM allowed two previously unknown deep-seated gravitational slope deformation (DGSD) bodies to be distinguished (Fig. 3d). The external body (no. 7 in Fig. 3d) extends approximately 3.40 km^2 with a W-E length of approximately 2200 m and a maximum N-S width of 2000 m. Its uppermost boundary, close to *Poggio Cocola* hill at approximately 300 m a.s.l., is delimited by recently developed trenches (no. 10 in the legend of Fig. 3). The internal DGSD body (n°8 in Fig. 3d) is within the larger one and has an extent of approximately 1.33 km^2. The two DGSD bodies are separated in the W by a topographic depression at approximately 260 m a.s.l., where abandoned and suspended paleo-drainages (no. 16 in the legend of Fig. 3) probably developed because of the different displacement rates of the two bodies. Both DGSD bodies are delimited to the E by the Simeto River, whose continuous erosion generates an escarpment affected by widespread shallow landslides (no. 9 in Fig. 3d).

The identified geomorphological features suggest that the kinematics of the two DGSD bodies are governed by deep-seated sliding surfaces, beginning at the top of the DGSD bodies in Fig. 3d and ending at the toe of the hill to the E, close to the Simeto River, as shown by the dashed red curves in Fig. 3e. The potential sliding surfaces are sub-planar, with a gentle slope, and involve a potential soil mass volume of approximately $3–4 \times 10^8$ m^3 with a mean thickness of approximately 100–150 m. The likely detachment is hypothesised to be at the interface between the brown brecciated clays (5a in Fig. 3e) and the grey-blue and brown marly clays (5b in Fig. 3e).

3.2. InSAR-derived ground displacements

The wrapped ascending and descending interferograms from S-1 data from December 22 to December 28, 2018, which span the volcanic inflation and earthquake dislocation, identified some local interferometric fringes 5 km west of Paternò village (the dashed black box in Figs. 1 and S2). Fringes are within the outer boundaries of both of the DGSD bodies identified by geomorphological analysis (the green border in Fig. 4a and b) and terminate abruptly at the foot of the hill (Fig. 4a and b). The ALOS-2 wrapped interferograms identify a similar pattern (Fig. S3a and b), but with a small number of fringes with respect to the S-1 data because of the different wavelength of the ALOS-2 SAR sensor (in Fig. S3, each colour cycle corresponds to ground displacements of approximately 11.45 cm along the SAR LoS).
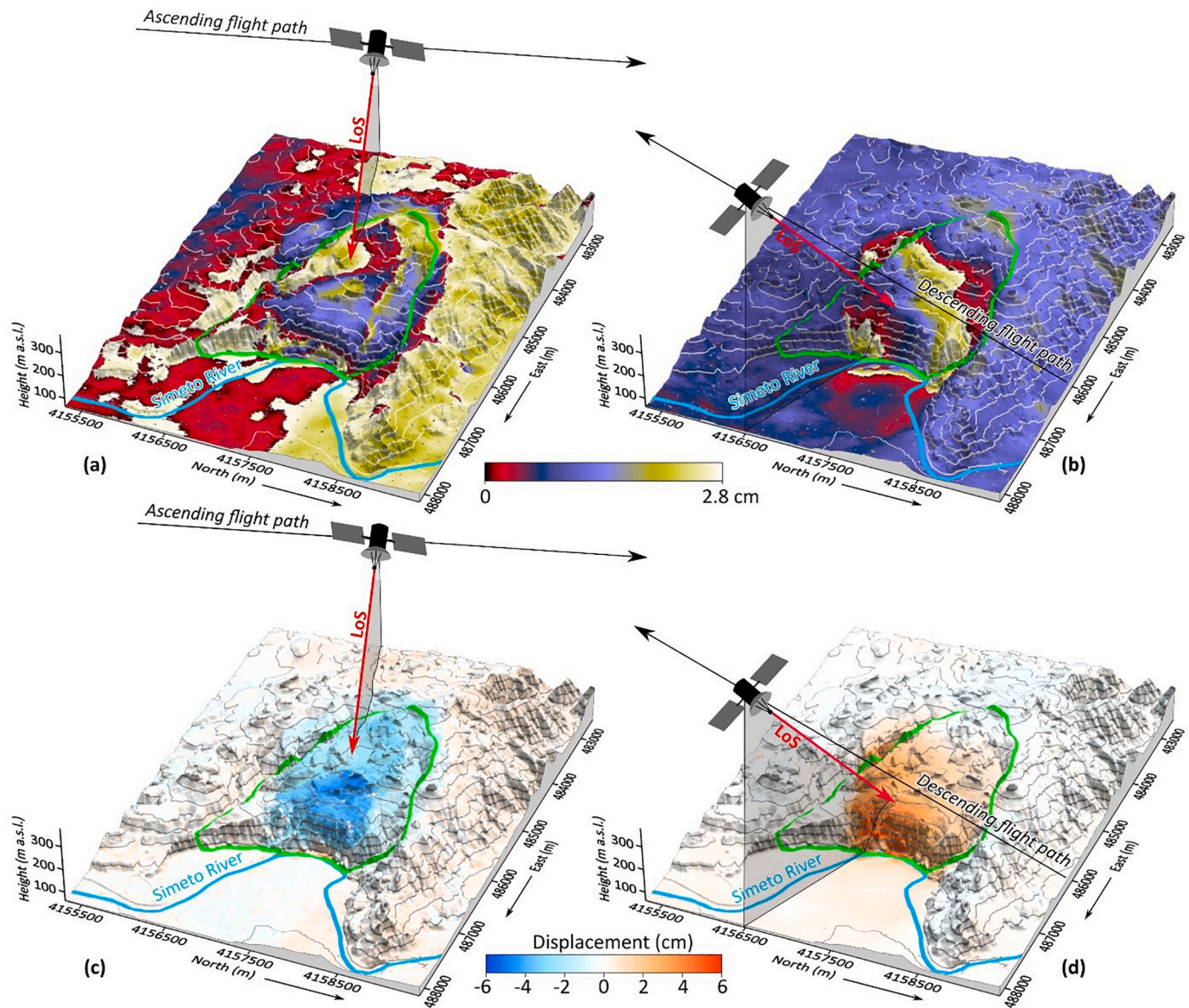
The ascending and descending S-1 interferograms dated December 16–22, before the volcanic eruption (Fig. S4a and b), do not identify any fringe patterns in the area. Therefore, the detected interferometric fringes in Fig. 4a and b identify localised ground movements accumulated during the seismic swarm (between December 22–28) that are thought to be related to processes occurring at shallow depths (Petley et al., 2002), such as reactivation of a single or multiple discrete sliding surfaces linked to the DGSD body. The latter was dormant before the volcanic eruption, as highlighted by multitemporal InSAR data from the literature (Fig. S4c) (Guglielmino et al., 2016) (http://tsd.ct.ingv.it/tsdws/sar/), which do not show significant movements over the study area in 2014–2017.

The unwrapped S-1 interferograms (Fig. 4c and d) show that displacements reach approximately 6 cm at the foot of the hill along both the descending and ascending orbits and gradually vanish towards the boundaries of the DGSD. The similarity of displacement amplitudes and spatial extents along satellite trajectories with different signs (negative and positive displacements indicate movements away from and towards the satellite sensor, respectively) suggest that horizontal displacements dominate the actual movement. Indeed, decomposition of the LoS displacements in the vertical and horizontal (E-W) components shows slight and uneven subsidence of the DGSD body reaching 2.5 cm (Fig. 5a and the red profiles in panels c and e) and a localised uplift of approximately 4 cm at the foot of the hill, close to the Simeto River. Horizontal displacements (Fig. 5b and the red profiles in panels d and f) are eastward-oriented, with amplitude increasing from W to E to a maximum of 7.5 cm. SAR sensors cannot observe N-S displacements because of the near-polar orbit of the satellite. However, these are negligible since geomorphological investigations indicate that the potential sliding surface of the DGSD is mainly eastward-oriented.

The combination of vertical and horizontal displacement components along the A-A' cross-section in Fig. 5g shows that the resultant displacement vectors along the DGSD body gradually increase in amplitude (vector length) and decrease in inclination (vector colouring) towards the E, consistent with the possible reactivation of both potential sliding surfaces identified from the geomorphological analysis (the dashed red curves in Fig. 3e and Fig. 5g). In detail, vectors are oriented downward and eastward at the top of the DGSD (i.e., at a distance of approximately 650 m in Fig. 5g) and are inclined at approximately 45°, indicating that the horizontal and vertical displacements are comparable. Moving towards the E, the vector inclination progressively decreases to approximately 10°, indicating an increase in the horizontal displacement amplitude with respect to the vertical displacement. An abrupt increase to 20° is identified at a distance of approximately 2100 m, probably associated with the reactivation of the second sliding surface. Displacement vectors invert the orientation from down to up and east near the Simeto River, indicating local bulging at the DGSD toe, in agreement with the hypothesis that the sliding surface ends at the toe of the hill.

The displacement of the DGSD is not limited to the investigated six-day timespan. Indeed, the horizontal and vertical displacement profiles from InSAR data along the A-A' and B-B' cross-sections (Fig. 5c to f) covering 12 days (the blue curve, from December 22, 2018 to January 03, 2019) and 18 days (the green curve, from December 22, 2018 to January 09, 2019) show that the DGSD accumulates further

Fig. 4. Processing results of the S-1 data in the time interval of December 22–28, 2018. The upper panels show the wrapped interferograms along the ascending (a) and descending (b) orbits, while the lower panels show the unwrapped interferograms, the displacement pattern along the ascending (c) and descending (d) orbits.

displacements, mainly in the eastward direction, at least until January 03, 2019 (the blue curve), but it does not accumulate further displacements on January 09, 2019. Such a displacement trend indicates that the slope movement is not instantaneous but is associated with the development and evolution of a transient phenomenon.

3.3. Earthquakes and strong-motion analysis

Most of earthquakes occurred in the period December 22–28, 2018 (Fig. 6a). In the same period, InSAR data show the maximum displacements of the DGSD (Fig. 5a and b). However, most of the events occurred more than 20 km from the DGSD area, and most had magnitudes less than 4 (Fig. 6a and b). Therefore, they did not release enough seismic energy to be detected at the PTR seismic station (the green triangle in Fig. 1 and 6b). Strong-motion data were recorded for only two earthquakes, the December 24 M_w 4.2 and December 26 M_w 4.9, events (Fig. 6a), which are approximately 25 km from the DGSD area. The first of these caused negligible ground shaking at the PTR seismic station, with a maximum horizontal PGA of roughly 0.003 g (D'Amico et al., 2020). The second event was the strongest of the sequence and caused

moderate-to-severe shaking intensity over an area of approximately 900 km² (Fig. 6b) (Faenza and Michelini, 2011, 2010).

On December 26, 2018 the PTR seismic station registered a PGA of 0.012 g and an energy content in terms of the Arias intensity (I_a) (Arias, 1970) of 0.438 cm/s on the *E*-W oriented acceleration component (Fig. 6b). This component aligns perfectly with the potential slip direction of the DGSD body (Fig. 3e).

Both the frequency and magnitude of earthquakes dropped drastically after December 28, 2018 (Fig. 6a). Therefore, it is unlikely that the displacements observed prior to January 03, 2019 (Fig. 5d to f) were caused by ground shaking. Instead, these were possibly related to a transient response after the strongest earthquake of the sequence, and associated with the geotechnical features of the soil mass.

3.4. Back-analysis of the DGSD

3.4.1. Assessment of the potential sliding plane and slip distribution

The InSAR-derived ground displacements were exploited to estimate the geometry, position and slip distribution of the potential sliding surface following the two-step inversion approach described in Section
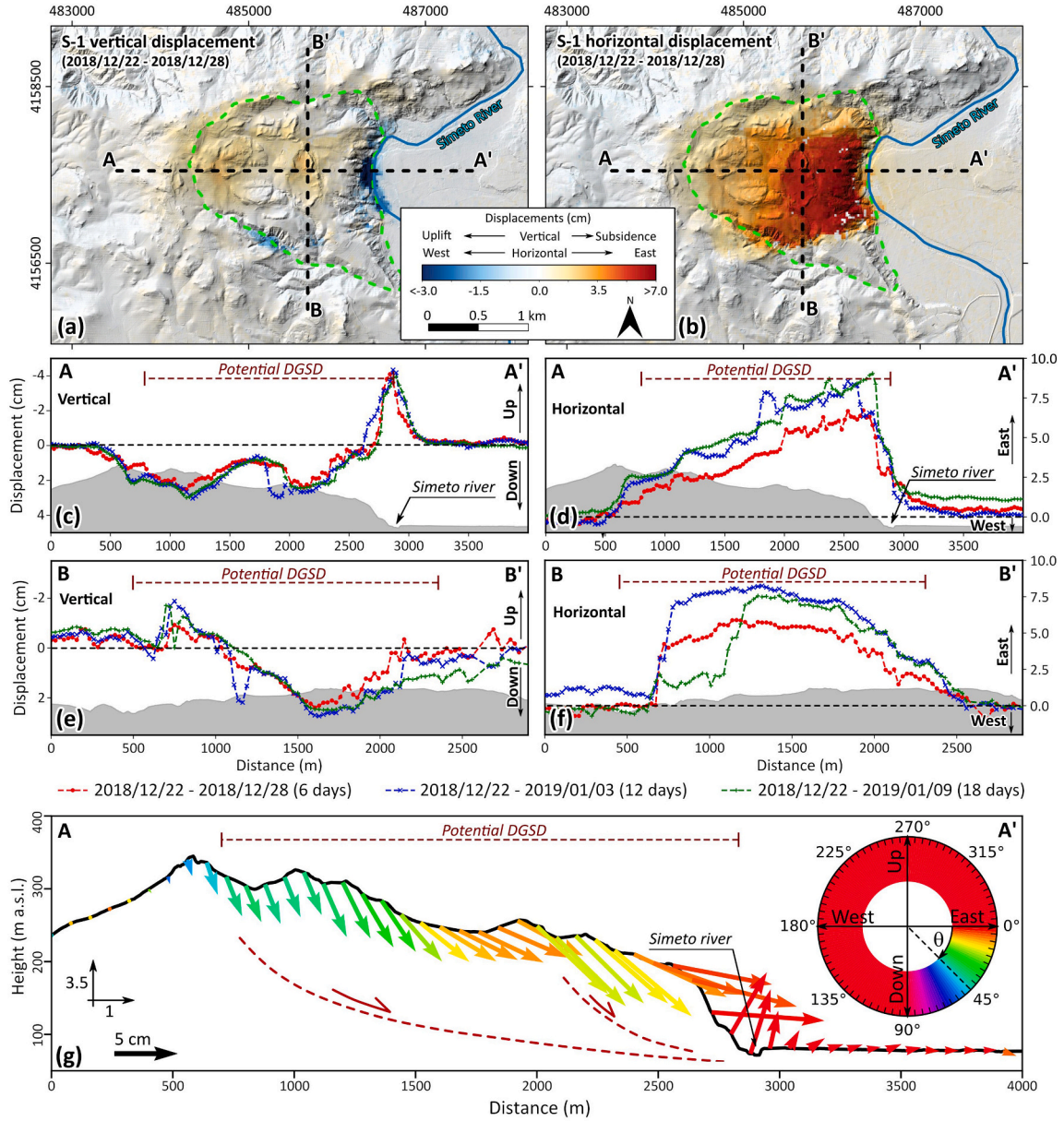
Fig. 5. Results of the decomposition of the ascending and descending S-1 InSAR displacements in the vertical and E-W components. (a) Vertical and (b) E-W displacement fields in the period December 22–28, 2018. Vertical and horizontal displacement profiles along the A-A' cross-section (panels c and d) and B-B' cross-section (panels e and f) from interferograms covering the time interval of December 22–28, 2018 (red curve), December 22, 2018 – January 03, 2019 (blue curve) and December 22, 2018 – January 09, 2019 (green curve). (g) Combined horizontal and vertical vector fields along the A-A' cross-section in Fig. 5a and b. The vector length indicates the displacement amplitude, the colour the vector inclination (θ). (For interpretation of the references to colour in this figure legend, the reader is referred to the web version of this article.)

2.4.1.

The geometry and position of the sliding plane are estimated by nonlinearly inverting the cumulative displacements from S-1 interferograms in the period December 22, 2018 - January 03, 2019 and the ALOS-2 interferograms in Fig. S3. The resulting slip plane (the red plane in Fig. S5a) is located below the DGSD boundary at an average height of approximately 90 m a.s.l. and has a length of 1450 m, a width of 1750 m, a dip of approximately 2.3° towards E, and a mean slip of approximately 10 cm directed towards the E (i.e., rake ≈ 100°). The assessment of the parameter uncertainty and trade-offs (Fig. S6) highlights that the plane geometry and position are well constrained (grey planes in Fig. S5a) and adequately reproduces the observed ground movements from both S-1 and ALOS-2 data, with RMSEs lower than 0.8 cm (Fig. S5b).

The slip distribution was estimated by discretising the sliding plane

retrieved from the nonlinear inversion step in a 150 m × 150 m grid (400 cells). Then, we linearly inverted the ascending and descending displacements from S-1 data, covering the period December 22–28, 2018 (left panels in Fig. 7a). These displacements are the best estimate of the coseismic movements caused solely by the December 26 M_w 4.9 event. The resulting slip distribution (Fig. 7b) is directed towards the E (green vectors in Fig. 7b, with a rake ≈ 100°), and its amplitude gradually increases from W to E (Section A-A' in Fig. 7b), peaking at approximately 8.5 cm at the foot of the hill. This slip distribution accurately reproduces the observed InSAR displacements from S-1 data (centre panels in Fig. 7a) with residuals lower than 1.5 cm and RMSEs smaller than 0.5 cm (right panels in Fig. 7a).
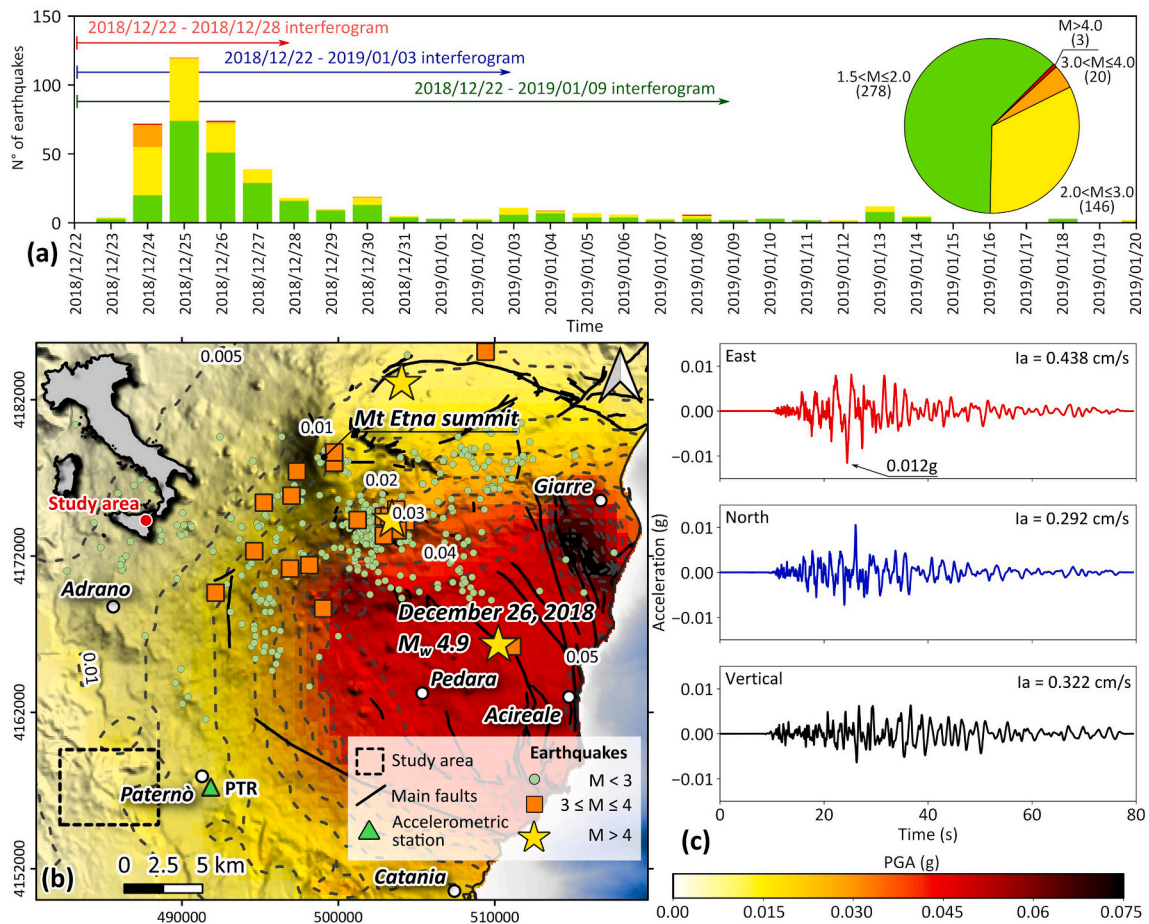
Fig. 6. Analysis of the earthquake sequence and strong-motion data. (a) Seismicity trend from December 22, 2018, to January 20, 2019, expressed as daily earthquakes and classified according to the magnitude. The red, blue and green arrows indicate the timespans covered by the S-1 interferograms analysed in Fig. 5 and listed in Table S1. (b) Map of the PGA produced by the December 26, 2018 M_w 4.9 earthquake, together with the spatial distribution of earthquakes recorded from December 23, 2018, to January 30, 2019 (Berardi et al., 2020). (c) Three components of the acceleration time history caused by the December 26, 2018 M_w 4.9 earthquake recorded at the PTR accelerometric station. (For interpretation of the references to colour in this figure legend, the reader is referred to the web version of this article.)

3.4.2. Infinite slope back-analysis and estimation of soil strength

After calculating the geometry and slip distribution (δ) of the potential sliding surface from the inversion of InSAR results, we estimated the critical soil strength parameters by performing a pseudostatic limit equilibrium analysis assuming an infinite slope (Fig. 2c).

The k_c values in eqs. (3) and (4) are estimated by calculating the critical acceleration (k_c) values that are compatible with the δ values for each cell of the sliding plane in Fig. 7b, following the procedure described in Section 2.4.2. First, we estimated the k_c-δ experimental relation (Fig. 8a) by selecting k_c values in the range of 1×10^{-5} g - 0.1 g and calculating the corresponding δ values with the Newmark displacement approach (Fig. 2a and b). We assumed the E-W component of the acceleration time history registered at the PTR station as the seismic input (Fig. 6b), with this component being the most energetic and perfectly aligned with the DGSD sliding plane orientation and slip direction (Fig. 7b). Then, from the obtained k_c-δ curve (Fig. 8a), we estimated the k_c values compatible with the δ values computed for each cell of the sliding plane in Fig. 7b. k_c values in the range of 0.0025 g - 0.006 g are estimated for the cells bounded by the external DGSD boundary (Fig. 8b). As expected, lower k_c values correspond to higher δ values.

Both drained and undrained conditions are assumed for the soil behaviour. For drained conditions, the critical friction angle (ϕ_c) is estimated using eq. (3) for each cell of the sliding plane in Fig. 7b, assuming a slope inclination (α) of 2.31° and the k_c values of Fig. 8b. The

computed ϕ_c values (Fig. 8c) range between 2.4 and 2.8 degrees, with a median value of approximately 2.5. These estimated values are not compatible with the experimental distribution of ϕ in Fig. 3b.

For undrained conditions, the critical undrained cohesion ($c_{u,c}$) is estimated according to Eq. (4) at each cell of the sliding plane in Fig. 7b. We assumed the k_c values in Fig. 8b, a slope inclination (α) of 2.31°, a soil unit weight (γ) of 19 kN/m³ (Fig. 3b) and a slope thickness (D) defined as the vertical distance between the ground surface and the centre of each cell on the sliding plane of Fig. 7b. The computed $c_{u,c}$ values (Fig. 8d) range between 30 and 200 kPa, with a median value of approximately 132 kPa. Such values are consistent with the experimental distribution of c_u shown in Fig. 3b.

4. Discussion

The pseudostatic, limit-equilibrium back-analysis of the landslide mass confirmed that the displacements detected by InSAR spanning December 22–28, 2018 (Fig. 4) were caused by the light-to-moderate seismic shaking from the December 26 M_w 4.9 earthquake. The earthquake triggered the undrained seismic instability of a previously unknown landslide mass that was dormant before the volcanic eruption (Fig. S7).

The computed critical undrained shear strength required to cause slope instability (the $c_{u,c}$ values in Fig. 8d) agrees with the experimental values obtained from geotechnical surveys (c_u boxplot in Fig. 3b).
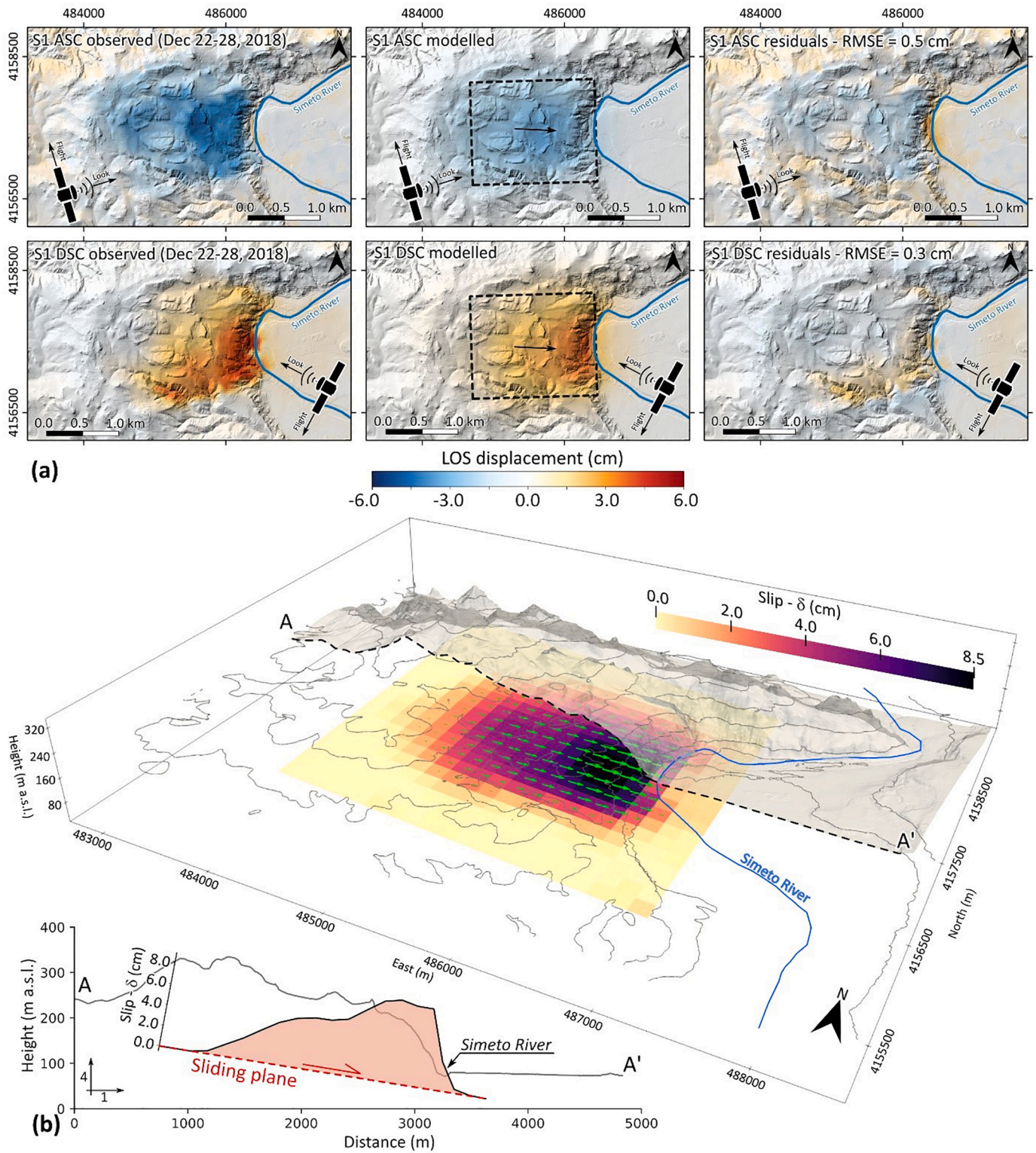
Fig. 7. Results of the analytical inversion of InSAR data. (a) Left panels: a stack of unwrapped ascending- and descending-track S-1 SAR interferograms spanning December 22–28, 2018. Centre panels: unwrapped best-fitting elastic dislocation model for distributed slip on a rectangular plane obtained from the inversion of InSAR outcomes. The dashed black rectangle shows the surface projection of the sliding plane, and the black arrow shows the direction of slip (rake). Right panels: unwrapped residuals between the data and the model. (b) 3D geometry and slip distribution of the potential sliding plane responsible for the ground displacements in panel a.

Conversely, the slope's seismic stability in drained conditions is guaranteed since the computed critical friction angles in drained conditions (the ϕ_c values in Fig. 8c) are very low, far below the experimental values (the ϕ boxplot in Fig. 3b).

The undrained behaviour of clay-like materials under cyclic loads (Ansal and Erken, 1989 and references therein) is caused by the increase in pore water pressure. Excess pore pressures develop because the applied seismic shaking velocity, together with the low permeability of
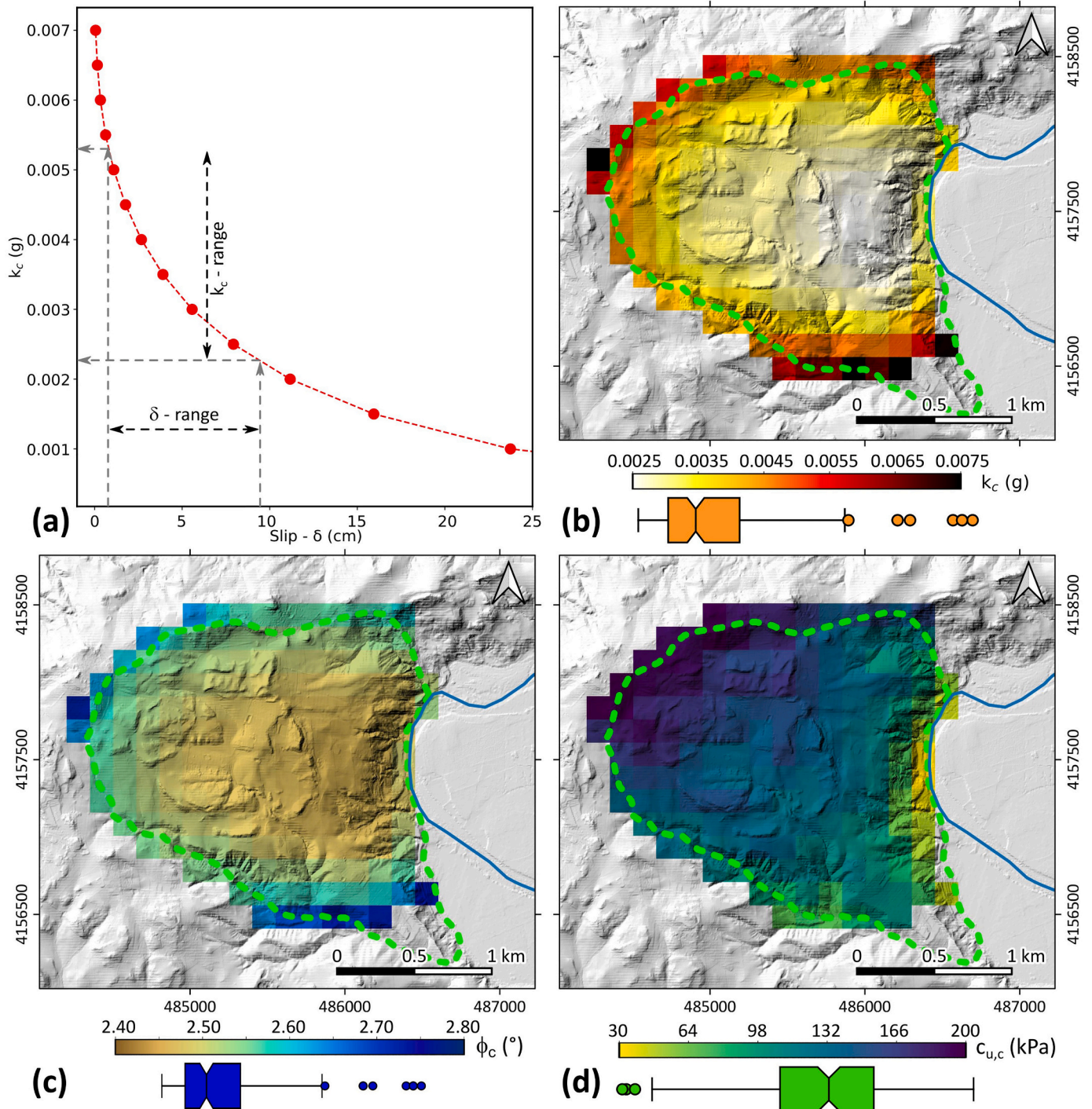
Fig. 8. Results of back-analysis for the infinite slope scheme. (a) Experimental k_c-δ curve estimated by applying the Newmark displacement approach with the *E*-W component of the acceleration time history in Fig. 6c. (b) Computed k_c values for each cell of the sliding plane in Fig. 7b. (c) Computed critical friction angle (ϕ_c) values for each cell of the sliding plane in Fig. 7b. (d) Computed critical undrained cohesion ($c_{u,c}$) values for each cell of the sliding plane in Fig. 7b.

cohesive soils, does not allow rapid fluid drainage and pore-pressure dissipation. For the Paternò landslide, the seismic shaking caused by the December 26, 2018, M_w 4.9 event developed excess pore pressures in the clay formation, which is characterised by low hydraulic conductivity (*k* in Fig. 3b) and by a saturation level close to 100% (*S* in Fig. 3b). Excess pore pressures caused undrained instability and the coseismic accumulation of ground displacements (Fig. 4c and d and Fig. 5a and b). The excess pore pressures that developed during seismic shaking dissipated in the days following the earthquake, allowing a gradual transition from unstable undrained behaviour to stable drained behaviour.

During this period, further displacements accumulated, as documented by the InSAR-derived ground movements (Fig. 5c to f). The latter highlight a progressive growth of mainly eastward-oriented displacement in the period December 22, 2018 – January 03, 2019, at a decreasing rate that likely mimics the pore pressure dissipation rate. Other transient phenomena, such as creep processes or heavy rains that could trigger surficial displacements, are unlikely. Indeed, multi-temporal InSAR data from 2014 to 2017 indicate that the DGSD mass was stable before the volcanic eruption and seismic swarm (Fig. S4c), thus excluding creep processes. Moreover, data collected at the Paternò

pluviometric station show that the amount of rain from December 22–28, 2018 was negligible (Fig. S8).

The earthquake epicentre position with respect to the landslide mass plays a fundamental role in landslide reactivation. The observed ground displacements are enhanced by alignment between the estimated slip plane (approximately W-E in Fig. 7) and the E-W acceleration component of the M_w 4.9 event registered at the PTR accelerometric station, which was the most energetic component of the earthquake (Fig. 6c). During an M_w 4.6 event that occurred on October 6, 2018 (Fig. S7), InSAR data do not identify any displacement over the DGSD body (Fig. S7). This discrepancy may be explained by the relative positions of the earthquake epicentre and the DGSD. The M_w 4.6 earthquake occurred approximately NNE of the Paternò landslide at an epicentral distance of only 10 km. Consequently, the N-S component of seismic shaking is the most energetic, with a PGA of 0.019 g (comparable with the PGA of the December 26, 2018 event). The E-W component had a PGA of only 2.69×10^{-5} (D'Amico et al., 2020), apparently is not enough to trigger landslide displacements in the W-E direction.

The adopted modelling approach and associated assumptions do not allow for a proper evaluation of excess pore pressures during seismic shaking and postseismic dissipation. The transient evolution of pore pressures is inferred from the undrained behaviour of the landslide mass only. Moreover, our modelling does not consider geometrical and lithological heterogeneities and rheological complexities, such as the non-planar shape of the sliding surface, the presence and mobilisation of multiple sliding surfaces (Fig. 3e and Fig. 5g) or soil layers with different geotechnical properties. Including such features, together with complete 3D dynamic numerical modelling accounting for the full coupling between solid deformation and fluid pressures, would provide a more comprehensive and accurate picture of the kinematics of the landslide mass during seismic shaking (Albano et al., 2015; Bottari et al., 2018), but it does not change the general conclusions provided in this work.

Despite the limitations of the modelling approach, there is good agreement between the results of the analysis and the geomorphological evidence. Indeed, the analytical inversion of InSAR data confirms that the observed ground displacements are caused by the sliding of a deep blind surface, the location and geometry of which agree with the surface hypothesised from geomorphological analyses (Fig. 3 and Fig. 7). This surface can be approximated with the infinite slope scheme adopted for the back-analysis and the surface lies approximately below the water surface height of the Simeto River (Fig. 7), thus confirming that the soil is completely saturated by water. Therefore, undrained behaviour of the clay-like soils composing the landslide mass is expected during seismic shaking.

The results of the analysis allowed us to identify the geometry and kinematics of a previously unknown landslide mass and confirm that even light-to-moderate earthquake shaking has a cumulative effect on landslides that does not necessarily manifest in the collapse of the landslide mass, but could potentially evolve into a catastrophic failure after several earthquakes. Identification of unknown quiescent landslide bodies can minimize the effects of their potential failure during an earthquake.

5. Conclusions

The interplay between volcano-tectonic earthquakes and the triggering of non-catastrophic landslide movement has been investigated by applying a multidisciplinary approach comprising geological, geomorphological, seismological and remote sensing data, together with analytical and dynamic modelling. The main conclusions of this study are:

- Geological and geomorphological analyses provided evidence of a previously unknown paleo-landslide located 5 km west of Paternò village and characterised by the presence of two distinct bodies, with an overall extent of approximately 3.40 km^2. The hypothetical

sliding surface starts at the toe of the hill and extends towards the top of the landslide mass at a depth of approximately 100–150 m from ground level.
- InSAR data show that the landslide mass, which was in a dormant phase, was reactivated during the Etna volcano eruption and the related seismic swarm.
- Analytical inversion of InSAR data identified the geometry and kinematics of the potential sliding surface. The geometry and position of the retrieved surface are in accordance with geological and geomorphological findings.
- Back-analysis of the observed ground displacements confirmed that the landslide mass reactivated during the light-to-moderate seismic shaking caused by the December 26 M_w 4.9 earthquake 25 km away. The earthquake caused undrained instability of the landslide and ground displacement.

Declaration of Competing Interest

The authors declare that they have no known competing financial interests or personal relationships that could have appeared to influence the work reported in this paper.

Appendix A. Supplementary data

Supplementary data to this article can be found online at https://doi.org/10.1016/j.rse.2021.112524.

References

Albano, M., Modoni, G., Croce, P., Russo, G., 2015. Assessment of the seismic performance of a bituminous faced rockfill dam. Soil Dyn. Earthq. Eng. 75, 183–198. https://doi.org/10.1016/j.soildyn.2015.04.005.
Albano, M., Saroli, M., M., M., Falcucci, E., Gori, S., Stramondo, S., Galadini, F., Barba, S., 2016. Minor shallow gravitational component on the Mt. Vettore surface ruptures related to Mw 6, 2016 Amatrice earthquake. Ann. Geophys. 59 https://doi.org/10.4401/ag-7299.
Albano, M., Polcari, M., Bignami, C., Moro, M., Saroli, M., Stramondo, S., 2017. Did anthropogenic activities trigger the 3 April 2017 mw 6.5 Botswana earthquake? Remote Sens. 9, 1–12. https://doi.org/10.3390/rs9101028.
Albano, M., Saroli, M., Montuori, A., Bignami, C., Tolomei, C., Polcari, M., Pezzo, G., Moro, M., Atzori, S., Stramondo, S., Salvi, S., 2018. The relationship between InSAR coseismic deformation and earthquake-induced landslides associated with the 2017 Mw 3.9 Ischia (Italy) earthquake. Geosciences 8, 303. https://doi.org/10.3390/geosciences8080303.
Ansal, A.M., Erken, A., 1989. Undrained behavior of clay under cyclic shear stresses. J. Geotech. Eng. 115, 968–983. https://doi.org/10.1061/(ASCE)0733-9410(1989)115:7(968).
Arias, A., 1970. Measure of earthquake intensity. In: Hansen, R.J. (Ed.), Seismic Design for Nuclear Power Plants. MIT Press, Cambridge MA, pp. 438–483.
Aryal, A., Brooks, B.A., Reid, M.E., 2015. Landslide subsurface slip geometry inferred from 3-D surface displacement fields. Geophys. Res. Lett. 42, 1411–1417. https://doi.org/10.1002/2014GL062688.
Atzori, S., Salvi, S., 2014. SAR data analysis in solid earth geophysics: from science to risk management, in: land applications of radar remote sensing. InTech. https://doi.org/10.5772/57479.
Atzori, S., Hunstad, I., Chini, M., Salvi, S., Tolomei, C., Bignami, C., Stramondo, S., Trasatti, E., Antonioli, A., Boschi, E., 2009. Finite fault inversion of DInSAR coseismic displacement of the 2009 L'Aquila earthquake (Central Italy). Geophys. Res. Lett. 36 https://doi.org/10.1029/2009GL039293.
Azzaro, R., Bonforte, A., Branca, S., Guglielmino, F., 2013. Geometry and kinematics of the fault systems controlling the unstable flank of Etna volcano (Sicily). J. Volcanol. Geotherm. Res. 251, 5–15. https://doi.org/10.1016/j.jvolgeores.2012.10.001.

Berardi, M., Battelli, P., Melorio, C., Modica, G., Thermes, C., Baccheschi, P., 2020. Bollettino Sismico Italiano (BSI), III quadrimestre 2018 (Version 1) [Data set]. https://doi.org/10.13127/BSI/201803.

Bignami, C., Salvi, S., Albano, M., Guglielmino, F., Tolomei, C., Atzori, S., Trasatti, E., Polcari, M., Puglisi, G., Stramondo, S., 2019. Multi-hazard analysis of Etna 2018 eruption by sar imaging. In: IGARSS 2019–2019 IEEE International Geoscience and Remote Sensing Symposium. IEEE, pp. 9314–9317. https://doi.org/10.1109/IGARSS.2019.8898695.

Bird, J.F., Bommer, J.J., 2004. Earthquake Losses Due to Ground Failure, 75, pp. 147–179. https://doi.org/10.1016/j.enggeo.2004.05.006.

Bonforte, A., Guglielmino, F., Puglisi, G., 2019. Large dyke intrusion and small eruption: the December 24, 2018 Mt. Etna eruption imaged by Sentinel-1 data. Terra Nova 31, 405–412. https://doi.org/10.1111/ter.12403.

Bottari, C., Albano, M., Capizzi, P., D'Alessandro, A., Doumaz, F., Martorana, R., Moro, M., Saroli, M., 2018. Recognition of earthquake-induced damage in the Abakainon necropolis (NE Sicily): results from geomorphological, geophysical and numerical analyses. Pure Appl. Geophys. 175, 133–148. https://doi.org/10.1007/s00024-017-1653-4.

Bozzano, F., Bretschneider, A., Esposito, C., Martino, S., Prestininzi, A., Scarascia Mugnozza, G., 2013. Lateral spreading processes in mountain ranges: insights from an analogue modelling experiment. Tectonophysics 605, 88–95. https://doi.org/10.1016/j.tecto.2013.05.006.

Branca, S., Coltelli, M., Groppelli, G., Lentini, F., 2011. Geological map of Etna volcano, 1:50,000 scale. Ital. J. Geosci. 130, 265–291. https://doi.org/10.3301/IJG.2011.15.

Carbone, S., Lentini, F., Branca, S., 2010. Note illustrative alla carta geologica d'Italia alla scala 1:50.000, Foglio 633, Paternò.

Casagli, N., Frodella, W., Morelli, S., Tofani, V., Ciampalini, A., Intrieri, E., Raspini, F., Rossi, G., Tanteri, L., Lu, P., 2017. Spaceborne, UAV and ground-based remote sensing techniques for landslide mapping, monitoring and early warning. Geoenviron. Disasters 4, 9. https://doi.org/10.1186/s40677-017-0073-1.

Chen, Q., Cheng, H., Yang, Y., Liu, G., Liu, L., 2014. Quantification of mass wasting volume associated with the giant landslide Daguangbao induced by the 2008 Wenchuan earthquake from persistent scatterer InSAR. Remote Sens. Environ. 152, 125–135. https://doi.org/10.1016/j.rse.2014.06.002.

Costantini, M., 1998. A novel phase unwrapping method based on network programming. IEEE Trans. Geosci. Remote Sens. 36, 813–821. https://doi.org/10.1109/36.673674.

Dalla Via, G., Crosetto, M., Crippa, B., 2012. Resolving vertical and east-west horizontal motion from differential interferometric synthetic aperture radar: the L'Aquila earthquake. J. Geophys. Res. Solid Earth 117. https://doi.org/10.1029/2011JB008689 n/a-n/a.

D'Amico, D., Felicetta, M., Russo, C., Sgobba, S., Lanzano, G., Pacor, F., Luzi, L., 2020. Italian Accelerometric Archive v 3.1. https://doi.org/10.13127/itaca.3.1.

De Novellis, V., Atzori, S., De Luca, C., Manzo, M., Valerio, E., Bonano, M., Cardaci, C., Castaldo, R., Di Bucci, D., Manunta, M., Onorato, G., Pepe, S., Solaro, G., Tizzani, P., Zinno, I., Neri, M., Lanari, R., Casu, F., 2019. DInSAR analysis and analytical modeling of Mount Etna displacements: the December 2018 volcano-tectonic crisis. Geophys. Res. Lett. 46, 5817–5827. https://doi.org/10.1029/2019GL082467.

Di Naccio, D., Kastelic, V., Carafa, M.M.C., Esposito, C., Milillo, P., Di Lorenzo, C., 2019. Gravity versus tectonics: the case of 2016 Amatrice and Norcia (Central Italy) earthquakes surface Coseismic fractures. J. Geophys. Res. Earth Surf. 124, 994–1017. https://doi.org/10.1029/2018JF004762.

Esposito, C., Martino, S., Mugnozza, G.S., 2007. Mountain slope deformations along thrust fronts in jointed limestone: an equivalent continuum modelling approach. Geomorphology 90, 55–72. https://doi.org/10.1016/j.geomorph.2007.01.017.

Faenza, L., Michelini, A., 2010. Regression analysis of MCS intensity and ground motion parameters in Italy and its application in ShakeMap. Geophys. J. Int. 180, 1138–1152. https://doi.org/10.1111/j.1365-246X.2009.04467.x.

Faenza, L., Michelini, A., 2011. Regression analysis of MCS intensity and ground motion spectral accelerations (SAs) in Italy. Geophys. J. Int. 186, 1415–1430. https://doi.org/10.1111/j.1365-246X.2011.05125.x.

Farr, T.G., Rosen, P.A., Caro, E., Crippen, R., Duren, R., Hensley, S., Kobrick, M., Paller, M., Rodriguez, E., Roth, L., Seal, D., Shaffer, S., Shimada, J., Umland, J., Werner, M., Oskin, M., Burbank, D., Alsdorf, D., 2007. The shuttle radar topography Mission. Rev. Geophys. 45, RG2004 https://doi.org/10.1029/2005RG000183.

Frattini, P., Crosta, G.B., Rossini, M., Allievi, J., 2018. Activity and kinematic behaviour of deep-seated landslides from PS-InSAR displacement rate measurements. Landslides 15, 1053–1070. https://doi.org/10.1007/s10346-017-0940-6.

Goldstein, R.M., Werner, C.L., 1998. Radar interferogram filtering for geophysical applications. Geophys. Res. Lett. 25, 4035–4038. https://doi.org/10.1029/1998GL900033.

Guglielmino, F., Bonforte, A., D'Agostino, M., Puglisi, G., 2016. Mt. Etna ground deformation imaged by SISTEM approach using GPS data and SENTINEL-1A TOPSAR data. In: ESA Living Planet Symposium. Prague. HAZA-113.

Huang, M.H., Fielding, E.J., Liang, C., Milillo, P., Bekaert, D., Dreger, D., Salzer, J., 2017. Coseismic deformation and triggered landslides of the 2016 mw 6.2 Amatrice earthquake in Italy. Geophys. Res. Lett. 44, 1266–1274. https://doi.org/10.1002/2016GL071687.

Jibson, R.W., 1993. Predicting earthquake-induced landslide displacements using Newmark's sliding block analysis. Transp. Res. Rec. 9–17.

Jibson, R.W., 2011. Methods for assessing the stability of slopes during earthquakes-a retrospective. Eng. Geol. 122, 43–50. https://doi.org/10.1016/j.enggeo.2010.09.017.

Jibson, R.W., Harp, E.L., Michael, J.A., 2000. A method for producing digital probabilistic seismic landslide hazard maps. Eng. Geol. 58, 271–289. https://doi.org/10.1016/S0013-7952(00)00039-9.

Kang, Y., Lu, Z., Zhao, C., Zhang, Q., Kim, J.-W., Niu, Y., 2019. Diagnosis of Xinmo (China) landslide based on interferometric synthetic aperture radar observation and modeling. Remote Sens. 11, 1846. https://doi.org/10.3390/rs11161846.

Keefer, D.K., 1984. Landslides caused by earthquakes. Bull. Geol. Soc. Am. https://doi.org/10.1130/0016-7606.

Lo Verme, S., La Mendola, F., 2007. Studio geologico ed indagini geognostiche per i lavori di completamenti del consolidamento aree a valle del centro abitato di Ravanusa.

Marquardt, D.W., 1963. An algorithm for least-squares estimation of nonlinear parameters. J. Soc. Ind. Appl. Math. 11, 431–441. https://doi.org/10.1137/0111030.

Massonnet, D., Feigl, K.L., 1998. Radar interferometry and its application to changes in the Earth's surface. Rev. Geophys. 36, 441–500. https://doi.org/10.1029/97RG03139.

Moro, M., Chini, M., Saroli, M., Atzori, S., Stramondo, S., Salvi, S., 2011. Analysis of large, seismically induced, gravitational deformations imaged by high-resolution COSMO-SkyMed synthetic aperture radar. Geology 39, 527–530. https://doi.org/10.1130/G31748.1.

Moro, M., Saroli, M., Gori, S., Falcucci, E., Galadini, F., Messina, P., 2012. The interaction between active normal faulting and large scale gravitational mass movements revealed by paleoseismological techniques: a case study from Central Italy. Geomorphology 151–152, 164–174. https://doi.org/10.1016/j.geomorph.2012.01.026.

Newmark, N.M., 1965. Effects of earthquakes on dams and embankments. Géotechnique 15, 139–160. https://doi.org/10.1680/geot.1965.15.2.139.

Okada, Y., 1992. Internal deformation due to shear and tensile faults in a half-space. Bull. Seismol. Soc. Am. 82, 1018–1040.

Parsons, B., Wright, T., Rowe, P., Andrews, J., Jackson, J., Walker, R., Khatib, M., Talebian, M., Bergman, E., Engdahl, E.R., 2006. The 1994 Sefidabeh (eastern Iran) earthquakes revisited: new evidence from satellite radar interferometry and carbonate dating about the growth of an active fold above a blind thrust fault. Geophys. J. Int. 164, 202–217. https://doi.org/10.1111/j.1365-246X.2005.02655.x.

Pepe, A., Calò, F., 2017. A review of interferometric synthetic aperture RADAR (InSAR) multi-track approaches for the retrieval of Earth's surface displacements. Appl. Sci. 7, 1264. https://doi.org/10.3390/app7121264.

Petley, D.N., Bulmer, M.H., Murphy, W., 2002. Patterns of movement in rotational and translational landslides. Geology 30, 719–722. https://doi.org/10.1130/0091-7613(2002)030<0719:POMIRA>2.0.CO;2.

Polcari, M., Montuori, A., Bignami, C., Moro, M., Stramondo, S., Tolomei, C., 2017. Using multi-band InSAR data for detecting local deformation phenomena induced by the 2016–2017 Central Italy seismic sequence. Remote Sens. Environ. 201, 234–242. https://doi.org/10.1016/j.rse.2017.09.009.

Polcari, M., Albano, M., Atzori, S., Bignami, C., Stramondo, S., 2018. The causative fault of the 2016 Mwp 6.1 Petermann ranges intraplate earthquake (Central Australia) retrieved by C- and L-band InSAR data. Remote Sens. 10, 1311. https://doi.org/10.3390/rs10081311.

Roback, K., Clark, M.K., West, A.J., Zekkos, D., Li, G., Gallen, S.F., Chamlagain, D., Godt, J.W., 2018. The size, distribution, and mobility of landslides caused by the 2015 Mw7.8 Gorkha earthquake, Nepal. Geomorphology 301, 121–138. https://doi.org/10.1016/j.geomorph.2017.01.030.

Rodríguez, C.E., Bommer, J.J., Chandler, R.J., 1999. Earthquake-induced landslides: 1980-1997. Soil Dyn. Earthq. Eng. 18, 325–346. https://doi.org/10.1016/S0267-7261(99)00012-3.

Sato, H.P., Une, H., 2016. Detection of the 2015 Gorkha earthquake-induced landslide surface deformation in Kathmandu using InSAR images from PALSAR-2 data. Earth Planets Sp. 68, 47. https://doi.org/10.1186/s40623-016-0425-1.

Stramondo, S., Trasatti, E., Albano, M., Moro, M., Chini, M., Bignami, C., Polcari, M., Saroli, M., 2016. Uncovering deformation processes from surface displacements. J. Geodyn. 102, 58–82. https://doi.org/10.1016/j.jog.2016.08.001.

Vecchio, E., 2011. Relazione geologica Esecutiva - Lavori di sistemazione ed ammodernamento della S.P. n. 109 ex S.R. n. 9 "Pietraperzia - Balata Mandreforte - Piano Sinopoli" e S.P. n. 96 "Pietraperzia - ponte Besaro". available at: http://www.provincia.enna.it/amministrazione-trasparente/bandi_gara_contratti/avvisi_Bandi_Inviti/contratti_lav_sottosoglia_com/2018/CIG_751196801A/3Studiogeologicoesecutivo.pdf.

Villani, F., Pucci, S., Azzaro, R., Civico, R., Cinti, F.R., Pizzimenti, L., Tarabusi, G., Branca, S., Brunori, C.A., Caciagli, M., Cantarero, M., Cucci, L., D'Amico, S., De Beni, E., De Martini, P.M., Mariucci, M.T., Messina, A., Montone, P., Nappi, R., Nave, R., Pantosti, D., Ricci, T., Sapia, V., Smedile, A., Vallone, R., Venuti, A., 2020. Surface ruptures database related to the 26 December 2018, MW 4.9 Mt. Etna earthquake, southern Italy. Sci. Data 7, 42. https://doi.org/10.1038/s41597-020-0383-0.

Williams, C.A., Wadge, G., 1998. The effects of topography on magma chamber deformation models: application to Mt. Etna and radar interferometry. Geophys. Res. Lett. 25, 1549–1552. https://doi.org/10.1029/98GL01136.

Zhang, Y., 2018. Review of Studies on Earthquake-Induced Landslides. Springer, Singapore, pp. 11–39. https://doi.org/10.1007/978-981-10-2935-6_2.